



Effects of size reduction on the structure and magnetic properties of core-shell Ni₃Si/silica nanoparticles prepared by electrochemical synthesis



Giancarlo Pigozzi^{a,*}, Debashis Mukherji^b, Yalçın Elerman^c, Pavel Strunz^d, Ralph Gilles^e, Markus Hoelzel^e, Bruno Barbier^f, Patrik Schmutz^a

^a Empa, Swiss Federal Laboratories for Materials Science and Technology, Überlandstrasse 129, 8600 Dübendorf, Switzerland

^b Institut für Werkstoffe, Technical University of Braunschweig, Langer Kamp 8, 38106 Braunschweig, Germany

^c Department of Engineering Physics, Faculty of Engineering, Ankara University, 06100 Besevler, Ankara, Turkey

^d Nuclear Physics Institute (NPI), 25068 Řež, Czech Republic

^e Technische Universität München, Forschungs-Neutronenquelle Heinz Maier-Leibnitz (MLZ), 85747 Garching, Germany

^f Steinmann Institut, Poppelsdorfer Schloss, 53115 Bonn, Germany

ARTICLE INFO

Article history:

Received 29 April 2013

Received in revised form 4 September 2013

Accepted 5 September 2013

Available online 14 September 2013

Keywords:

Intermetallics

Nanostructured materials

Transition metal alloys and compounds

Electrochemical synthesis

Crystal structure

Magnetic measurements

ABSTRACT

Nanostructured nickel silicides find application in electronics, high-temperature alloys, electrode materials and catalysis. In this work, the effect of size reduction on the structure and magnetic properties of β_1 -Ni₃Si intermetallic phase nanoparticles is studied. Electrochemical selective phase dissolution (ESPD) was used to produce the β_1 -Ni₃Si nanoparticles of different sizes (from 20 to 215 nm) by extracting β_1 nano-size precipitates from two-phase Ni–Si and Ni–Si–Al precursor alloys. The extracted nanoparticles have a core-shell structure with β_1 -Ni₃Si core and an amorphous silica shell. Particles size and shape are controlled by the composition and thermal treatment of the precursor alloys. Precipitates size is scaled without modifying the ordered L1₂ lattice structure. The bulk β_1 -Ni₃Si is ferromagnetic below 260 K with low saturation magnetization (2 emu/g), while the core-shell Ni₃Si/silica nanoparticles are superparamagnetic at low temperatures (<9–11 K) with low coercivity (<90 Oe) and magnetization >20 emu/g at 5 T. It is suggested that weak particle magnetic moments and low magnetic anisotropy of the L1₂ structure are responsible for these properties. The shell on one hand protects the core from degradation; however the oxidation of the core/shell interface region can influence the magnetic behavior of the nano-powders.

© 2013 Elsevier B.V. All rights reserved.

1. Introduction

Transition metal silicides based on iron, cobalt and nickel constitute an important class of compounds for technological applications. In addition to their use as high-temperature structural materials, metal silicides have been identified as very promising candidates for micro-/nano-electronic devices. Silicides are usually refractory materials with high melting point which possess high strength and high resistance to oxidation and corrosion. They also have narrow bandgap and low electrical resistivity. Transition metal silicides (e.g., NiSi, TiSi₂, CoSi₂) are now widely used in the semiconductor industry and they are very important to complement

metal-oxide semiconductor (CMOS) devices as ohmic contacts, interconnects and gates [1]. In particular, nickel silicides have low electrical resistivity and noble metal-like properties which make these silicides promising candidates for applications as electrode materials [2] as well as in hydro-desulfurization catalysis [3].

Ni₃Si is a L1₂ structured (ordered face centered cubic) intermetallic compound and possesses anomalous yield strength as a function of temperature, and specially, it shows excellent strength and good oxidation resistance at temperatures up to 700 °C [4]. Owing to the unique range of properties, including excellent thermal stability, the metal-rich silicide Ni₃Si has been identified as a promising candidate for several applications (high temperature energy conversion equipment or as gate in nano-electronics devices [5,6]). According to the binary Ni–Si phase diagram, β_1 -Ni₃Si has no congruent melting point but is formed by solid-state (eutectoid and peritectoid) reactions of monoclinic β_2 -Ni₃Si or hexagonal γ -Ni₅Si₂ phases [7]. Synthesis of single phase Ni₃Si alloy is therefore not straightforward. However, different routes are available for the

* Corresponding author. Tel.: +41 58 765 48 27.

E-mail addresses: giancarlo.pigozzi@empa.ch (G. Pigozzi), d.mukherji@tu-bs.de (D. Mukherji), Yalcin.Elerman@ankara.edu.tr (Y. Elerman), strunz@ujf.cas.cz (P. Strunz), Ralph.Gilles@frm2.tum.de (R. Gilles), markus.hoelzel@frm2.tum.de (M. Hoelzel), b.barbier@uni-bonn.de (B. Barbier).

synthesis of Ni_3Si nanostructures, for example synthesis of freestanding Ni_3Si nanowires by high temperature chemical reaction in gas has been recently reported [1]. There were also attempts to produce nano-scale Ni_3Si by other routes, e.g. by elemental blending of Ni and Si powders through mechanical alloying [8]. Also, it has been demonstrated in a previous publication by the authors that nanoparticles of Ni_3Si can be produced from two phase Ni–Si alloys by electrochemical selective phase dissolution process [9] and these particles resist to temperatures up to 1000 °C [10].

Nickel/silicon heterostructures and Ni–Si based nanostructured alloys are used in many devices. Nickel silicide phases may be formed at interfaces between nickel and silicon when subjected to heat. In particular, Ni_3Si phase can appear in Ni/Si heterostructures during processes which are, for example, commonly used in electronic applications (e.g., ion-beam mixing and thermal annealing of Ni/Si multilayered films [11] or Ni silicidation of polycrystalline-Si/SiO₂ gates [12]). The physical properties of such systems can be therefore affected by the presence of Ni_3Si .

While many investigations on electronic properties of Ni_3Si nanostructures are found in literature, magnetic properties of Ni_3Si have drawn less attention. Some nickel silicides (Ni_2Si , NiSi , and NiSi_2) have been found to be ferromagnetic at room temperature [13]. However, due to non-continuous changes of the electronic density of Ni silicides with Si content, the behavior of Ni_3Si cannot be directly inferred from properties of other silicides. Few reports on magnetic properties of bulk Ni_3Si are found in literature (see e.g. [14,15]). However, the chemical structure and magnetic behavior of Ni_3Si are of fundamental interest as they can be different at the nano-scale and it is therefore important to characterize them.

In this paper, a fundamental investigation of the size reduction effect for Ni_3Si particles and its influence on their crystal structure, morphology and magnetic properties is presented. It is demonstrated that nanoparticles of the Ni_3Si phase are superparamagnetic at low temperatures, if they can be produced at sizes below ~200 nm. All presented results are obtained from core–shell type Ni_3Si nanoparticles, where the ordered crystalline core is magnetic and the shell is constituted of an amorphous Si-oxide mantel. A shell surrounding the nanoparticles plays an important role in protecting the core from environmental degradation. There is a growing scientific and technological interest in superparamagnetic nanoparticles due to their applications in magnetic resonance imaging, hyperthermia and drug delivery [16]. Capping the particles with an inert biocompatible shell is a necessity and ways how to control shell composition and thickness on the nano-scale are of great general relevance. However, the shell can have an influence on the magnetic properties of the powder and therefore affect the performance in applications. In this work an indication of how the magnetic characteristics of investigated Ni_3Si nano-powders are influenced by the silica shell is also provided and this will be the subject of further investigations.

2. Experimental

2.1. Materials

Ni_3Si nanoparticles of different sizes were prepared by electrochemical selective phase dissolution (ESPD) technique – extracting them from two-phase Ni–Si alloys. In the present work, two Ni–Si-based alloys (one with and the other without ternary element aluminum addition) are investigated (see Table 1). The nanoparticles obtained by extraction of the Ni_3Si precipitates from these alloys are further characterized (details of particles are reported in Table 2). Firstly, nano-sized precipitates of the Ni_3Si -type intermetallic phase are grown to different desired sizes in the solution heat treated two-phase Ni–Si-based alloys by first homogenization at 1100 °C for 48 h and water quenched followed by annealing treatment (ageing) at 600 °C for different times (4–24 h). Afterwards, the alloy is subjected to an electrochemical anodic polarization (selective electro-etching) inducing dissolution of the corrosion susceptible matrix and extraction of the nano-precipitates. This

process was performed by placing a two-phase alloy sample in an electrolytic cell. The cell includes a Pt counter electrode, a Calomel reference electrode (SCE, potential +0.244 V_{SHE}) and a plate-like sample of the alloy as anode (working electrode). Electrochemical experiments were performed using a potentiostat (PGSTAT30 from the company Metrohm-Autolab). As electrolyte, an aqueous solution containing 1% citric acid and 1% ammonium sulfate (pH value 2.5) was used. The ESPD electrochemical processing was performed potentiostatically by holding an extraction voltage between 1.0 and 1.25 V versus SCE at room temperature. The optimal potential giving the highest selectivity between high matrix dissolution rate and nanoparticle production for a given alloy can be first determined by performing electrochemical potentiodynamic polarization scans. After the extraction, the precipitate particles are then collected from the aqueous solution forming the nano-powders described in the present work. Further details of the synthesis were reported in a previous publication [9].

Table 1 not only reports the composition of the alloys NS1 and NS2 (referred to as precursor alloys in this work) from which the nanoparticles are extracted, but it also includes the detail of the heat treatments. Different ageing times were applied on the two alloys with the purpose of producing different sizes of nano-precipitates. A third alloy (NS3) was also prepared to characterize the bulk properties of the Ni_3Si phase. Instead of the stoichiometric 25 at.% Si, the composition of NS3 was chosen as Ni–22.5Si (at.%) in order to avoid formation of unwanted $\gamma\text{-Ni}_5\text{Si}_2$ phase richer in Si. This alloy was annealed differently than the precursor alloys (heat treatment details in Table 1). Table 2 shows details about the investigated nano-powder samples (composition, size); with reference to the precursor alloys they are extracted from. In both cases, the extracted nanoparticles have a core–shell structure. Although two different alloy compositions are used (different Al and Si amounts), this variation has no consequences on the crystal structure of the Ni_3Si precipitate phase which maintains the L₁₂ structure.

2.2. Characterization methods

2.2.1. Structure

Both the precursor alloys and the nano-powders were characterized by diffraction methods. X-ray diffraction (XRD) measurements were made on a high resolution Siemens D 5000 powder diffractometer with a focusing graphite monochromator in front of the scintillation counter, set up in the Bragg–Brentano geometry [18]. Measurements were done on solid samples with Cu K α radiation (doublet: $\lambda_{\text{Cu1}} = 1.54056$ Å, $\lambda_{\text{Cu2}} = 1.54439$ Å) in the angular range 2 θ –130° and a 2 θ step of 0.02°. Neutron powder diffraction (ND) measurements were performed at the high-resolution-Powder Diffractometer (SPODI) [19,20] in the Heinz-Meier-Leibnitz neutron source (MLZ) at the Technical University of Munich. The powder samples were placed in a niobium container and special care was taken to align the powder in the neutron beam. A Ge 551 monochromator with 0.1549 nm neutron wavelength (λ) was used for these measurements. Morphology and composition of the bulk alloys and nanoparticles were investigated in a FEI Nova Nano-SEM 230 Scanning electron microscope (SEM) equipped with Oxford X-Max Energy Dispersive X-ray (EDX) system and a Jeol JEM 2200FS transmission electron microscope (TEM), operating at 200 kV. The TEM was equipped with a field emission source, an Omega[®] energy filter and EDX detector. Small-Angle Neutron Scattering (SANS) measurements were carried out using the SANS-II instrument at the spallation neutron source (SINQ), at the Paul Scherrer Institute (Villigen, Switzerland) [21]. Scattering data were collected at several geometries by varying the sample-detector distance from 1.2 m to 6 m at two neutron wavelengths (λ) of 6.3 Å and 10.5 Å. The full covered range of scattering vector magnitude (Q) was 1.5×10^{-3} Å⁻¹–0.13 Å⁻¹. To further characterize the core–shell structure of the Ni_3Si nanoparticles, contrast variation measurements were also performed by SANS [22]. The very different neutron scattering lengths of hydrogen and deuterium are exploited in this SANS experiment. This technique has also been applied in the past to characterize core–shell structures [17,23,24]. The nanoparticles were dispersed either in D₂O or in H₂O or in ethanol (in which the particles are usually stored) and eventually in different mixtures of D₂O and ethanol. The measured raw SANS data were corrected for background scattering from the particular solvent or mixture of solvents and converted to an absolute scale using the SASFit software [25]. The particle size distribution (PSD) is obtained by fitting the scattering profile data with the theoretical scattering profile of a distribution of spherical particles having a core–shell structure. The distributions of core diameter and shell thickness are varied in the model in order to match the experimental results (see Ref. [17] for more details on SANS data reduction).

2.2.2. Magnetic properties

Direct Current (DC) magnetic field measurements of the temperature-dependent and field-dependent magnetization were carried out at the Ankara University. The temperature range between 5 and 300 K was investigated with a Physical Properties Measurement System (PPMS) and Magnetic Properties Measurement System (MPMS) from Quantum Design. In PPMS, the DC measurements were made in zero field cooled (ZFC) and field cooled (FC) sequences with cooling/heating rate of 2.5 K/s. The room temperature magnetic measurements were performed using the Vibrating Sample Magnetometer-VSM (EV9 from MicroSense) with cooling/heating sequences in 5 K steps. The magnetization of the powder samples were first measured in the ZFC mode, whereby the samples were first cooled from 350 K to 5 K

Table 1
Details of the solid samples.

Alloy ID	Composition (at.%)	Solution treatment	Ageing
NS1 ^a	Ni–13.3Si–2.0Al	1100 °C/24 h/WQ ^b	600 °C/24 h/WQ ^b
NS2 ^a	Ni–14.5Si	1100 °C/4 h/WQ ^b	600 °C/4 h/WQ ^b
NS3	Ni–22.5Si	1050 °C/48 h/950 °C/48 h/FC ^c	600 °C/24 h/FC ^c

^a Precursor alloy.^b WQ = water quenched.^c FC = furnace cooling.**Table 2**
Details of the powder samples.

Powder ID	Precursor alloy	Phases	Mean size (nm)
Ni3Si-1	NS1	Ni ₃ Si(Al) core, SiO ₂ shell	93 and 215 (bimodal) ^a
Ni3Si-2	NS2	Ni ₃ Si core, SiO ₂ shell	20

^a See Ref. [17].

in the absence of the magnetic field. Then, the magnetic field was applied and the data were collected during the temperature increase scan up to 300 K. Subsequently, without removing the magnetic field, FC measurements were made during decreasing temperature back to 5 K. As last step, the magnetization was measured in a field-heated (FH) mode by increasing temperature again without removing the magnetic field.

3. Results and discussion

3.1. Structure and phase content of bulk alloys

After the ageing heat treatment, a two-phase microstructure with intermetallic Ni₃Si precipitate dispersed in a Ni(Si) solid solution matrix is obtained for the NS1 and the NS2 precursor alloys.

The SEM images in Fig. 1a and b are obtained from polished and etched precursor alloys (NS1 and NS2) and show the distribution of the Ni₃Si(Al) and Ni₃Si precipitates, respectively, on the sample surface after the ageing heat treatment. Fig. 1c shows the microstructure of the nearly single phase NS3 alloy. The β_1 -Ni₃Si phase (dark gray grains) is the dominant phase in NS3 and a low amount of residual Ni rich solid solution phase (light gray areas) is also present, mainly at the grain boundaries. This heterogeneity is resulting from the non-stoichiometric composition of the alloy. However, the majority of intermetallic grains in NS3 alloy have the L1₂ structure and no γ -Ni₅Si₂ phase was found (see diffraction results below, Fig. 2c). The composition of these grains was measured by EDX as Ni–24.6(5) at.% Si, which is compatible with Ni₃Si. Fig. 1d schematically depicts the morphology of the Ni₃Si phase in the investigated alloys. While the NS1 alloy has a bimodal precipitate distribution, the precipitates are unimodally distributed in the NS2 alloy.

The phase content, the crystal structure and the lattice constant of the precipitate particles in the precursor alloys were characterized by X-ray and neutron diffraction. The ND pattern from the solid sample (NS1) is presented in Fig. 2a. The pattern contains all allowed reflections from the fcc matrix phase Ni(Si,Al). The large penetration depth of neutrons, which weakly interacts with the matter, allows probing a large volume of the solid sample and makes the powder-like pattern in the nanostructured solid sample possible. The superlattice reflections indicate the presence of the second phase in the alloy with L1₂ crystal structure, corresponding to Ni₃Si-type precipitate particles. The lattice constant of the Ni₃Si-type precipitates in the NS1 alloy is determined as 0.35175(20) nm, while that of the Ni(Si,Al) matrix solid-solution phase is 0.35204(15) nm. The corresponding lattice misfit is –0.08% (calculated using the formula $2(a_p - a_m)/(a_p + a_m)$, where a_p and a_m are the lattice constant for the precipitate and the matrix, respectively).

Fig. 2b displays a XRD pattern from the solid sample of the NS2 alloy. This sample is polycrystalline with large grains, therefore it was first aligned in the diffractometer in order to obtain the

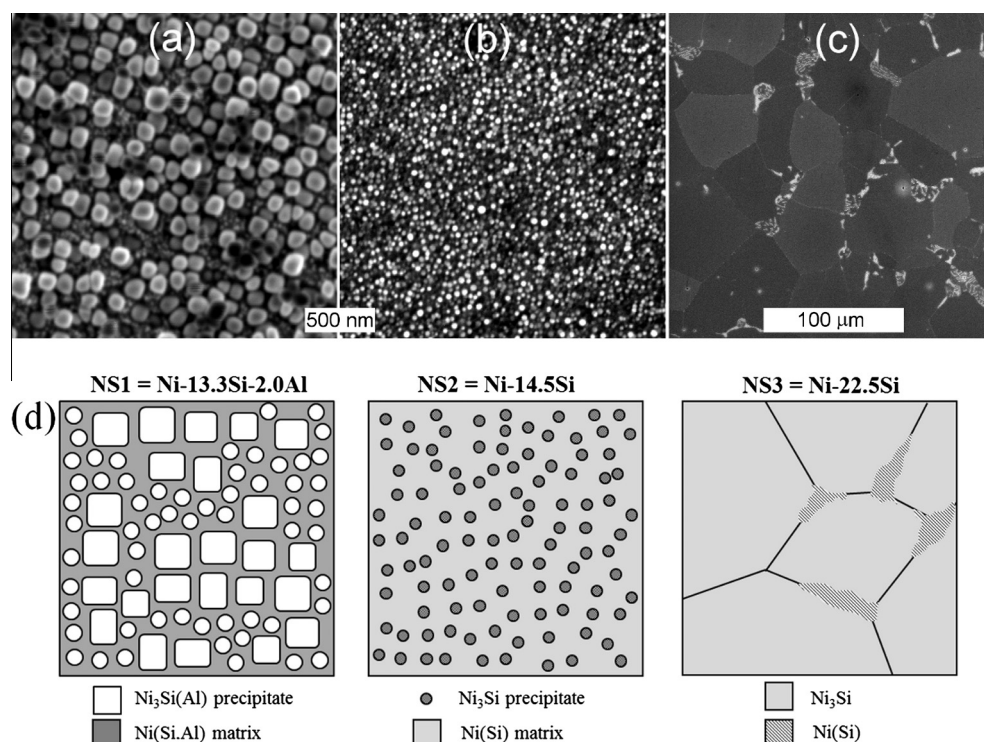


Fig. 1. SEM images of the alloys. Etched surface of (a) heat treated NS1 alloy showing the Ni₃Si(Al) precipitates, (b) NS2 alloy showing the Ni₃Si precipitates and (c) NS3 alloy. (d) Schematic diagram depicting the different phases of the alloys NS1, NS2 and NS3.

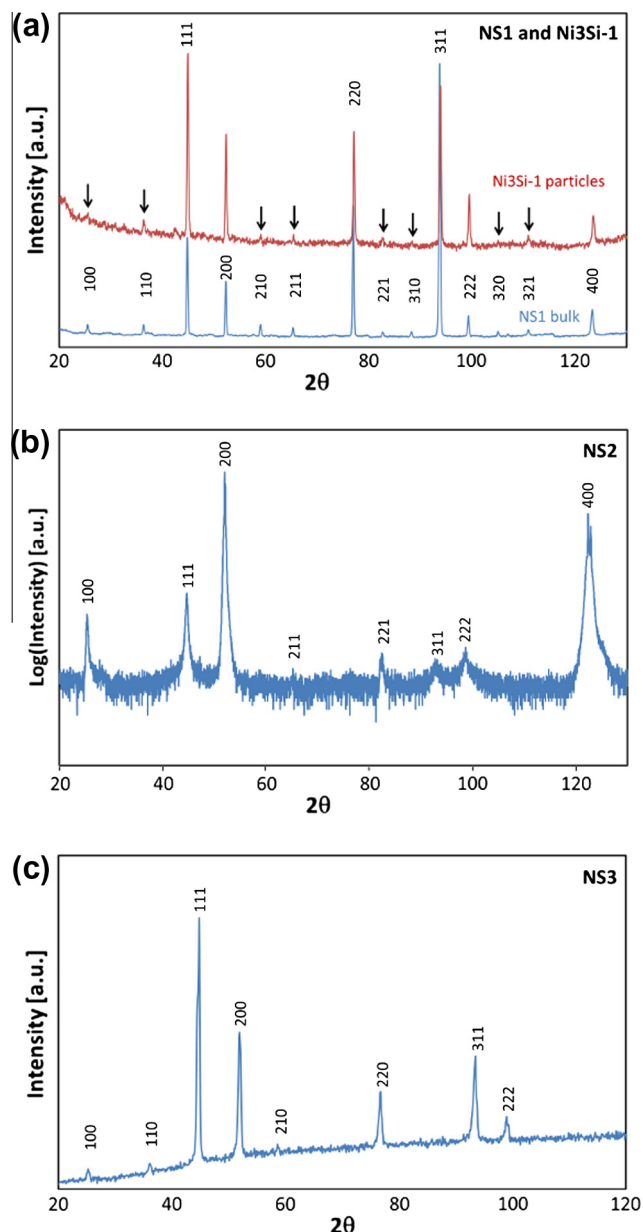


Fig. 2. Diffraction patterns from alloys and nanoparticles. (a) Neutron diffraction profiles recorded from the NS1 alloy and from the corresponding extracted Ni₃Si(Al) nanoparticles (powder sample Ni₃Si-1). The arrows in (a) indicate the L1₂ superlattice reflections from the Ni₃Si(Al) precipitate phase. (b) X-ray diffraction profile (log scale) recorded from the NS2 alloy. (c) X-ray diffraction profile recorded from the NS3 alloy.

maximum intensity of the $h00$ peaks ($h = 1, 2, 3, 4$) before recording the θ – 2θ diffraction scan. It also confirms a two phase structure and the presence of Ni₃Si phase precipitates with the L1₂ crystal structure embedded in the Ni(Si) solid solution matrix. The lattice constant of the Ni₃Si phase precipitates and the matrix phase was determined as 0.35175(20) nm and 0.35243(15) nm, respectively from the 100, 200 and 400 peaks of the XRD pattern in Fig. 2b. The corresponding lattice misfit in NS2 alloy is –0.19%.

Fig. 2c displays the XRD pattern from a solid sample of the alloy NS3. It contains reflections from the large β_1 -Ni₃Si phase grains and the lattice constant value is 0.3510(2) nm. A very small volume of the Ni(Si) solid-solution retained in this alloy as isolated islands along grain boundaries (Fig. 2c) does not significantly contribute to the XRD pattern.

3.2. Structure and morphology of nanoparticles before and after extraction

Intermetallic precipitates in the precursor alloys NS1 and NS2 have been extracted by the ESPD method [9,26], and nanoparticles of Ni₃Si(Al) and Ni₃Si phase are obtained, respectively. The extracted nano-powders have different particle size distributions corresponding to the precipitate in the precursor alloys. Additionally, a thin amorphous silica shell covering the nanoparticles is formed in situ during the electrochemical extraction process [9]. Details of the investigated core-shell powder samples are reported in Table 2.

The structure and composition of Ni₃Si-1 nano-powder was previously characterized by TEM/EDX and was presented in an earlier publication (Ni₃Si(Al) in Ref. [12]). The neutron diffraction pattern of the Ni₃Si-1 powder is displayed in Fig. 2a (top pattern). It shows reflections corresponding to the L1₂ crystal structure. The lattice constant of extracted Ni₃Si(Al) nanoparticles (Ni₃Si-1) as measured by X-ray and neutron diffraction is 0.35094(3) nm.

Energy-filtered transmission electron microscopy (EF-TEM) was used to characterize the Ni₃Si-2 nano-powder extracted from NS2 alloy. The bright-field transmission electrons image in Fig. 3a shows a typical sample of the Ni₃Si-2 nanoparticles, which also have a core shell structure (Fig. 3b). The particle size of Ni₃Si-2 powder is much finer compared to the Ni₃Si-1 nanoparticles (see Fig. 1 in Ref. [9]). The elemental distribution map as measured by EF-TEM of the core and the shell of the Ni₃Si-2 nanoparticles is shown in Fig. 3c, which is color coded (Si = blue, O = red, Ni = green). Relatively large particles within the nano-powder were chosen for this analysis in order to increase the detected signal. It is seen that the core contains Ni and Si, while the shell is a mixture of O and Si. The powder diffraction pattern in Fig. 2d displays reflections corresponding to the L1₂ phase; however, rings are not continuous due to the low number of particles illuminated by the electron beam. These results confirm that the Ni₃Si-2 nanoparticles have analogous core-shell structure like the Ni₃Si-1 nanoparticles previously investigated [9,17].

The extracted core-shell nanoparticles were characterized by small angle neutron scattering (SANS) and their particle size distribution (PSD) was calculated. Fig. 4 shows the azimuthally averaged neutron scattering intensity of the Ni₃Si-2 nanoparticles dispersed in a mixture of H₂O and D₂O and the calculated particle size distribution (core + shell), determined from the fitting of the neutron intensity profile. The estimated mean particle sizes of the extracted Ni₃Si-1 and Ni₃Si-2 particles are listed in Table 2. The size distribution obtained from SANS for the bimodal Ni₃Si-1 nanoparticles extracted from NS1 alloy was reported in Ref. [17] as 93 nm and 215 nm for the smaller and larger populations, respectively. The Ni₃Si-2 presented in detail in this paper has been optimized to have smaller mean particle diameter (20 nm, core + shell) and a narrower size distribution.

Shell thickness of the two samples (Ni₃Si-1 and Ni₃Si-2) was also measured from the SANS experiment and both types of particles have different shell thicknesses. The bimodal Ni₃Si-1 particles have a shell thickness of 17 nm for the larger and 5 nm for the smaller size population, respectively [17]. In the Ni₃Si-2 powder, the smaller size nanoparticles also have a thinner shell of only 3 nm thickness. Therefore, the shell thickness scales with the particle size. This size effect can be explained by considering the anodic polarization to which the precursor alloy is subject during precipitates extraction for the nanoparticles synthesis, whose details are reported in Ref. [9]. During the ESPD process, the time a precipitate particle remains attached to the precursor alloy is proportional to its size. A thicker oxide shell can therefore form around larger particles as they keep an electric contact with the precursor alloys for longer time. This scaling effect was found for

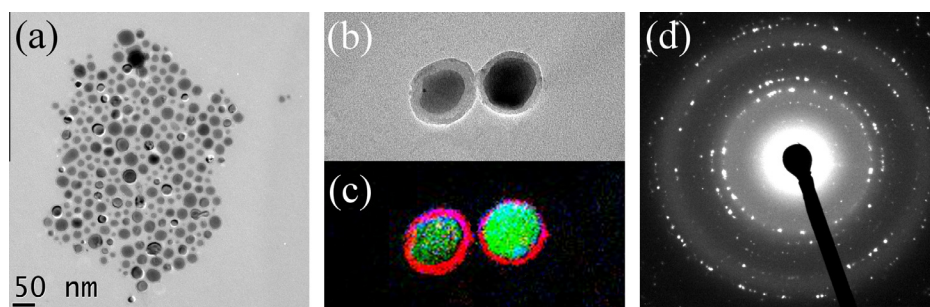


Fig. 3. Transmission electron micrographs of Ni_3Si nanoparticles (powder sample $\text{Ni}_3\text{Si-2}$) extracted from the alloy NS2. (a) Bright-field TEM of a group of particles. (b) Electron energy loss map of selected particles in (c) displaying the chemical distribution of elements in the nanoparticles (blue = Si, red = O, green = Ni). (d) Selected area electron powder diffraction pattern of nanoparticles in (a). (For interpretation of the references to color in this figure legend, the reader is referred to the web version of this article.)

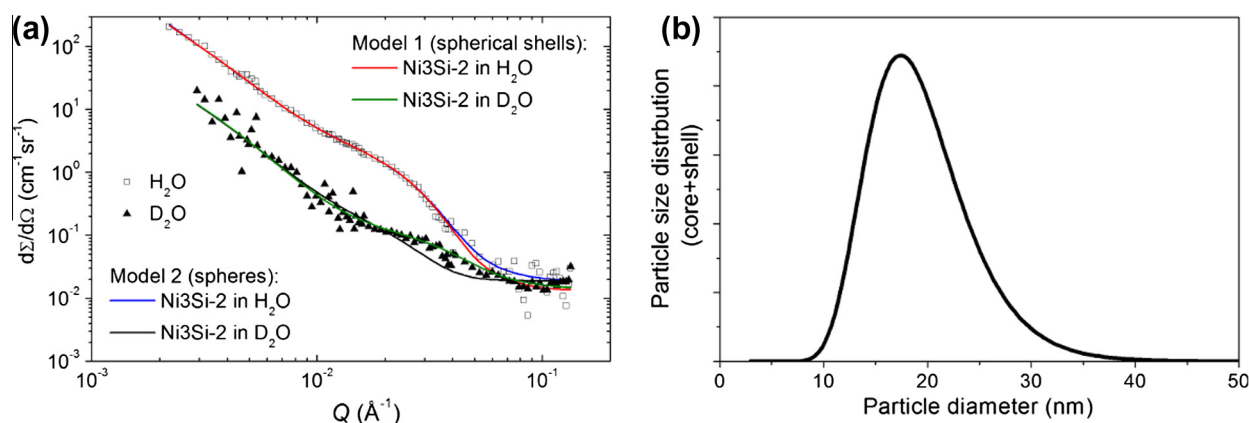


Fig. 4. Small angle neutron diffraction of $\text{Ni}_3\text{Si-2}$ core-shell nano-powders. (a) Azimuthally averaged neutron scattering profile from nanoparticles dispersed in a mixture of $\text{H}_2\text{O}/\text{D}_2\text{O}$. Square and triangle symbols indicate data from H_2O and D_2O , respectively. Continuous lines represent calculated profile according to two models. Model 1, distribution of spherical shells added to clusters and incoherent scattering; Model 2, distribution of spheres added to clusters and incoherent scattering. (b) Calculated particle size distribution (core + shell).

particles of different dimensions in the same alloy (a solely oxidation effect in solution can therefore be excluded) as well as in different alloys NS1 and NS2.

The morphology and composition of the nanoparticles core can be controlled in the solid state by tuning composition (thereby elastic mismatch) and heat treatment of the precursor alloy. In alloys with coherent second phase precipitates (e.g., Ni-base superalloys with Ni_3Al precipitates (γ') embedded in Ni(Al) solid solution (γ) matrix), the two phases have different lattice constants and the precipitate particles can be accommodated coherently in the matrix only with the creation of an inhomogeneous elastic strain field around them. It must be noted that the elastic strain field not only depends on the difference in the lattice constants between the matrix and the precipitate phases, but also strongly depends on the size of the precipitate inclusions. It is also well known that the lattice misfit influences precipitate size and morphology in Ni-superalloys [27]. In many commercial Ni-base superalloys the lattice misfit between γ' and γ phases is negative. Further, the relatively large cuboidal γ' precipitates (with ~ 500 nm size) are harder than the matrix γ phase therefore the elastic strain is mostly accommodated in the matrix. A negative elastic misfit value indicates that the lattice of the precipitates is expanded and the one of the matrix is contracted at the precipitate matrix interface, in order for them to match coherently. In the investigated NS1 and NS2 alloys (analogous to the Ni-superalloys with L_{12} Ni_3Al precipitates) the precipitates sizes are much smaller (< 200 nm). Also the Ni_3Si precipitates in the two alloys have the same measured lattice constant (see Table 3), but there is a significant difference in the

elastic misfit as determined from the diffraction experiments (the observed misfit is -0.08% for NS1 and -0.19% for NS2, respectively). This difference in misfit is due to the different lattice constant measured for the solid solution matrix phase in the two alloys (i.e. $0.35204(15)$ nm for NS1 and $0.35243(15)$ for NS2; see Table 3). It is not clear if this is due only to the different matrix composition which arises with the addition of Al in NS1. There may also be a contribution to the elastic strain due to the different size of the Ni_3Si precipitates in the two alloys (Table 2). In the present study, the same lattice constant is determined for the Ni_3Si precipitates embedded in NS1 and NS2 precursor alloys. The precipitate sizes in both alloys are too small to determine their chemical composition accurately in the bulk. The composition of precipitates extracted from NS1 alloy was measured by TEM/EDX and demonstrated that these nanoparticles contain up to 3.3 at.% Al [9]. The lattice constant of the extracted $\text{Ni}_3\text{Si(Al)}$ powder (from precursor alloy NS1) measured by XRD and by electron powder diffraction (EPD) in TEM was $0.35094(3)$ nm and $0.3513(3)$ nm, respectively and the lattice constant of extracted Ni_3Si nanoparticles (from precursor alloy NS2) measured by EPD was $0.3506(3)$ nm [5]. This also show that the two extracted nanoparticles [Ni_3Si or $\text{Ni}_3\text{Si(Al)}$] have the same lattice constant. It is therefore more likely that the difference of precipitate size in NS1 and NS2 alloys has a stronger influence on the lattice misfit values determined presently, rather than the influence of the precipitate composition.

The elastic misfit between solid solution matrix and intermetallic precipitates has a significant influence on the precipitate particle shape as well. For alloys with small misfit (below $\sim 0.5\%$ [27])

Table 3

Lattice parameters of the alloys and the nanoparticles phases.

Alloy ID	L1 ₂ (nm)	fcc (nm)	Misfit (%)	Extracted precipitates (nm)		Contraction after extraction (%)
NS1	0.35175(20)	0.35204(15)	−0.08	Ni3Si-1	0.35094(3)	−0.23
NS2	0.35175(20)	0.35243(15)	−0.19	Ni3Si-2	0.3506(3)	−0.32
NS3	0.3510(2)	–	–	–	–	–

smaller precipitates maintain a spherical shape (observed for NS2 and of smaller population in NS1 in this work), while during coarsening the precipitates may change shape and assume a more faceted shape like cuboidal (observed for the larger precipitate population in NS1 alloy in this work) or even become plate-like. The equilibrium shape of precipitates deviates from sphere during coarsening as a consequence of the elastic strain energy minimization [27]. In the present case, larger precipitate particles (~200 nm) in NS1 alloy attain a cuboidal shape while smaller particles (~80 nm) maintain the spherical shape (see Fig. 1 and Table 2). Precipitates in NS2 alloy which are much smaller (~20 nm) still maintain a spherical shape, despite a larger lattice misfit.

It may be pointed out that after extraction from the alloy, the nanoparticles are relaxed and are free of any strain [10]. Precipitates in bulk alloys NS1 and NS2 have a larger unit cell than bulk β_1 -Ni₃Si because of the lattice expansion originated from the coherency. After the precipitates are extracted the lattice constant is, however, compatible with the bulk β_1 -Ni₃Si phase reported in literature (0.351 nm [28]). Once the matrix is dissolved by ESPD process, any elastic constrain is removed and particle core relaxes to a smaller lattice constant without changing the crystal structure. Also the amorphous shell around the nanoparticles does not provide any mechanical constrain. It was therefore demonstrated that the control on composition and heat treatment of the precursor alloy is successful in downscaling precipitate size and in tuning their morphology without significantly modifying the lattice or the composition. Nanoparticles of different sizes but with same structural characteristics can be therefore produced by ESPD extraction; thereby the effects of size reduction on magnetic properties of extracted nanoparticles can be studied.

3.3. Magnetic properties of the bulk alloys

Fig. 5a and b show the temperature-dependent and field-dependent magnetization of the annealed precursor alloys NS1, NS2 and the nearly single phase (β_1 -Ni₃Si) NS3 alloys. All the alloys display soft magnetic properties with high permeability. A paramagnetic to ferromagnetic transition is observed at different temperatures below 273 K in all alloys. The NS1 alloy has a Curie temperature of 235 K and the magnetization reaches the saturation value (about 8 emu/g) under 0.1 T at 173 K. The NS2 alloy has a Curie temperature of 198 K and the magnetization reaches the saturation value (about 49 emu/g) under 0.1 T at 183 K. The NS3 alloy is also ferromagnetic at lower temperatures, however the paramagnetic to ferromagnetic transition is not as sharp as in NS1 and NS2 alloys. The magnetization at 100 Oe starts a progressive increase around 265 K, and it is apparent that its Curie point ranges between 230 and 260 K. The magnetization of NS3 alloy reaches the saturation value above ~1 Tesla at 170 K.

According to literature (e.g., in Ref. [14]), experimental data on Curie temperature of nickel alloys are scattered. Upon addition of up to 11 at.% Si (i.e. the solubility limit of Si in Ni at room temperature) the Curie point of Ni linearly drops from 630 K to a value in the range of ~150–200 K (the values reported in literature scatters between 153 and 198 K [14], which then represent a drop of 478 and 433 K). The Curie temperature then remains constant for

compositions up to 18 at.% Si (i.e. in the two phase alloys), as long as the L1₂ Ni₃Si precipitate phase is present. The magnetic moment of nickel, instead decreases (also linearly) beyond the solubility limit with addition of up to 15 at.% Si, indicating a dependence on the proportion of fcc/L1₂ phases in the alloy. For the NS2 alloy, which has 14.5 at.% Si, the Curie point was determined as 189 K in the present study, which agrees with the value reported in the literature. Low amount of Al (2 at.%) was added to the alloy NS1 in order to change the second phase particles morphology as discussed above. In general, aluminum addition has a strong effect on the magnetization of bulk nickel alloys and in particular on their Curie temperature. The addition of 2 at.% Al to pure Ni (which is much below the 10 at.% solubility limit of Al in Ni at 673 K) results in the drop of Curie temperature to ~573 K (~60 K lower than in pure Ni [14]). The Curie temperature measured on the ternary Ni–13.3Si–2Al alloy NS1 studied here was 235 K (i.e. 396 K below that of pure nickel). This represents a significantly lower drop in Curie point compared to a consideration of pure additive behavior of Al plus Si. Furthermore, the saturation magnetization decreases with increasing addition of mixed alloying elements (Si and Al) in the three investigated alloys. A more rapid drop than a purely linear behavior is observed, clearly indicating that the effect on the magnetic properties of Ni–Si(–Al) alloys cannot be explained on the basis of linear combination of alloying additions.

As the data in Table 4 show, the saturation magnetization M_s sharply decreases with decreasing Ni content in the alloy. Further, by observing how the M_s value in the 3 alloys scales with % strain, it is apparent that the strain induced in the alloy due to elastic misfit between precipitate and matrix phases may have an influence on the saturation magnetization. On the other hand, the mechanically harder precipitate particles in the alloys accumulate the same amount of strain and their composition is not significantly different in the two alloys. Moreover, precipitates become ferromagnetic at much lower temperatures (see below, Section 3.4). It can be therefore concluded that the nickel rich fcc solid solution matrix phase is responsible for the ferromagnetic character of these alloys.

3.4. Magnetic properties of the nanoparticles

Fig. 6a shows the ZFC and FC magnetization curves of the Ni₃Si-1 nanoparticles between 3 and 350 K in an applied field of 50 Oe. At 9 K, the ZFC curve starts dropping and this temperature corresponds to the blocking temperature (T_B). Fig. 6b displays the field-dependent magnetization curves for Ni₃Si-1 nanoparticles recorded at different temperatures between 5 and 300 K. The magnetization value at 5 T decreases from 22.3 emu/g (at 5 K) to 0.5 emu/g (at 300 K) with increasing temperature. A small ferromagnetic hysteresis is observed at 5 K with a coercivity of 90 Oe (see inset in Fig. 6b). The ZFC and FC magnetization curves of the Ni₃Si-2 nanoparticles between 3 and 40 K, in an applied field of 100 Oe, are displayed in Fig. 6c. The ZFC curve separates from the FC curve at 11 K and then starts to increase again at lower temperatures (~5 K) indicating the blocking temperature (T_B) for Ni₃Si-2 nanoparticles is 11 K and the particles are ferromagnetic below this temperature. Fig. 6d shows the field-dependent magnetization curves for Ni₃Si-2 nanoparticles recorded at different temperatures between 5 and 150 K. The measured coercivity value H_C is

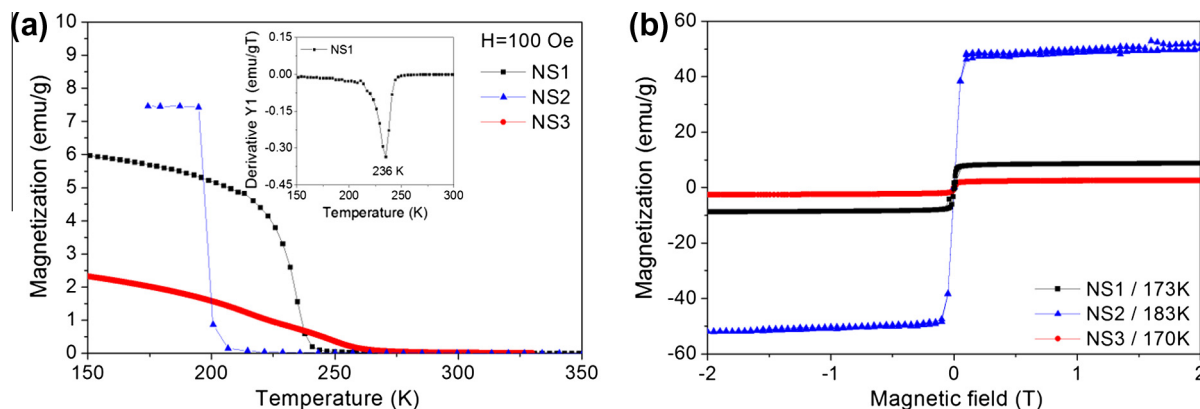


Fig. 5. Magnetization of bulk alloys. (a) Temperature dependent magnetization of the NS1, NS2 and NS3 alloys at 100 Oe. (b) Field dependant magnetization curves of NS1 at 173 K, NS2 at 183 K and NS3 at 170 K recorded below their respective Curie points.

Table 4
Summary of magnetic properties of the investigated alloys.

Alloy name	Ni content (at.%)	Curie point (K)	Saturation magnetization (emu/g)	Elastic misfit strain (%)
NS2	85.5	198	49	−0.19
NS1	84.7	235	8	−0.08
NS3	77.5	230–260	2	–

10 Oe at 5 K. The magnetization value at 5 T decreases with increasing temperature from 23.2 emu/g at 5 K to 0.8 emu/g at 150 K.

Magnetic exchange interaction between silica shell and magnetic core is not expected, but the non-magnetic silica shell partially suppresses the overall magnetic signal of the nanoparticles. However, it does not change the magnetic character of the core except reducing the overall magnetization that could be measured. The nano-powder samples contain a distribution of particle size; therefore, the magnetic moments are distributed accordingly. As the magnetization response of the powder is a superposition of contributions from particles of different sizes, the magnetization curves diverge from the theoretical Langevin function, which is rigorously valid only for mono-dispersed particles. Particles in the Ni₃Si-2 powder having smaller diameter carry in average a lower magnetic moment compared to the Ni₃Si-1 powder. This is reflected in the field-dependent magnetization curves (see Fig. 6b and d). A steep increase in magnetization at low fields for the Ni₃Si-1 sample (Fig. 6b) can be attributed to the presence of larger particles in this powder sample which carry larger magnetic moments and are more easily aligned by the external field. In contrast, the powder sample of Ni₃Si-2 with smaller particles shows a more gradual increase of the magnetization at low fields (Fig. 6) as smaller moments (smaller particles) are not easy to align.

It is known that when a bulk ferromagnetic material is reduced to nano-size, single-domain magnetism dominates and the magnetic properties of the material may be changed. The ordered transition metal intermetallic compounds (like Ni₃Al and Ni₃Ga) with L₁₂ crystal structure are typically paramagnetic at room temperature and have a ferromagnetic transition at low temperatures (e.g. 30 or 40 K as reported for Ni₃Al in [29] or [30], respectively). The nano-sized Ni₃Si and Ni₃Si(Al) precipitates in the precursor alloys also have an ordered L₁₂ crystal structure and this ordered structure is retained in the extracted nano-powders Ni₃Si-1 and Ni₃Si-2. The Ni₃Si phase has cubic symmetry and it exhibits low magneto-crystalline anisotropy [30], therefore the blocking of the magnetic moments on sample cooling is expected to occur at very

low temperatures. The blocking temperature for the two nano-powder samples Ni₃Si-1 and Ni₃Si-2 are observed at about 9 K and 11 K, respectively (Fig. 6a and c) and therefore both nano-powders are superparamagnetic at the low temperatures (<9 K or <11 K, respectively). For the two investigated superparamagnetic powders, the characteristic time scale of thermal fluctuations of the particle moment about the magnetic easy axis drops below the time scale of measurement (few seconds) at the blocking temperature, causing the particle magnetic moment to drop. Moreover, no tendency of saturation was observed even up to a field of 5 T for both the nano-powder samples, as one would expect for an assembly of superparamagnetic particles [31].

Important differences are observed in the two investigated nano-powders. For the Ni₃Si-1 nanoparticles, the FC and ZFC curve start to separate around 215 K (see inset in Fig. 6a). Similar behavior was observed in superparamagnetic CoPt nanoparticles by Rakshit et al. [31] and it is attributed to the agglomeration of particles. The magnetic moment drop at 9 K is quite pronounced for the Ni₃Si-1 particles (Fig. 6a). In this sample, a complete blocking is achieved below 9 K and the particles switch from paramagnetic to ferromagnetic with a coercivity of about 90 Oe, as demonstrated by the M(H) curve at 5 K (Fig. 6b). On the other hand, for the Ni₃Si-2 nanoparticles, the ZFC curve slightly decreases and separates from the FC curve at temperatures below 11 K. According to the M(H) curve at 5 K (Fig. 6d), Ni₃Si-2 sample has soft ferromagnetic properties with very low coercivity (10 Oe). Because of this, the difference between ZFC and FC curve is small below the blocking temperature. The transition observed in the Ni₃Si-2 nano-powder is also not as sharp as that in the Ni₃Si-1 sample. This can be due to inter-particle interactions that are expected to increase the blocking temperature and give rise to a spread of the blocking point over different temperatures, thereby broadening the temperature range over which the transition takes place.

As the temperature is decreased further, the difference between the two curves progressively becomes smaller and both FC and ZFC curves increase continuously down to 3 K. Below T_B the ferromagnetic hysteresis of these nanoparticles is very narrow. A possible explanation of this behavior below T_B is given by superposition of the ferromagnetic component of the particle core over a paramagnetic component. The paramagnetic contribution may originate from impurities at the core-shell interface which achieve magnetic order at low temperature [32]. Impurities are possibly included at the core-shell interface during the nanoparticles synthesis in the electrolyte. Alternatively, a paramagnetic component can also be present in the sample as a consequence of a composition spread in the nanoparticles, where less Ni-rich particles would behave more paramagnetic. Moreover, the silica shell thickness

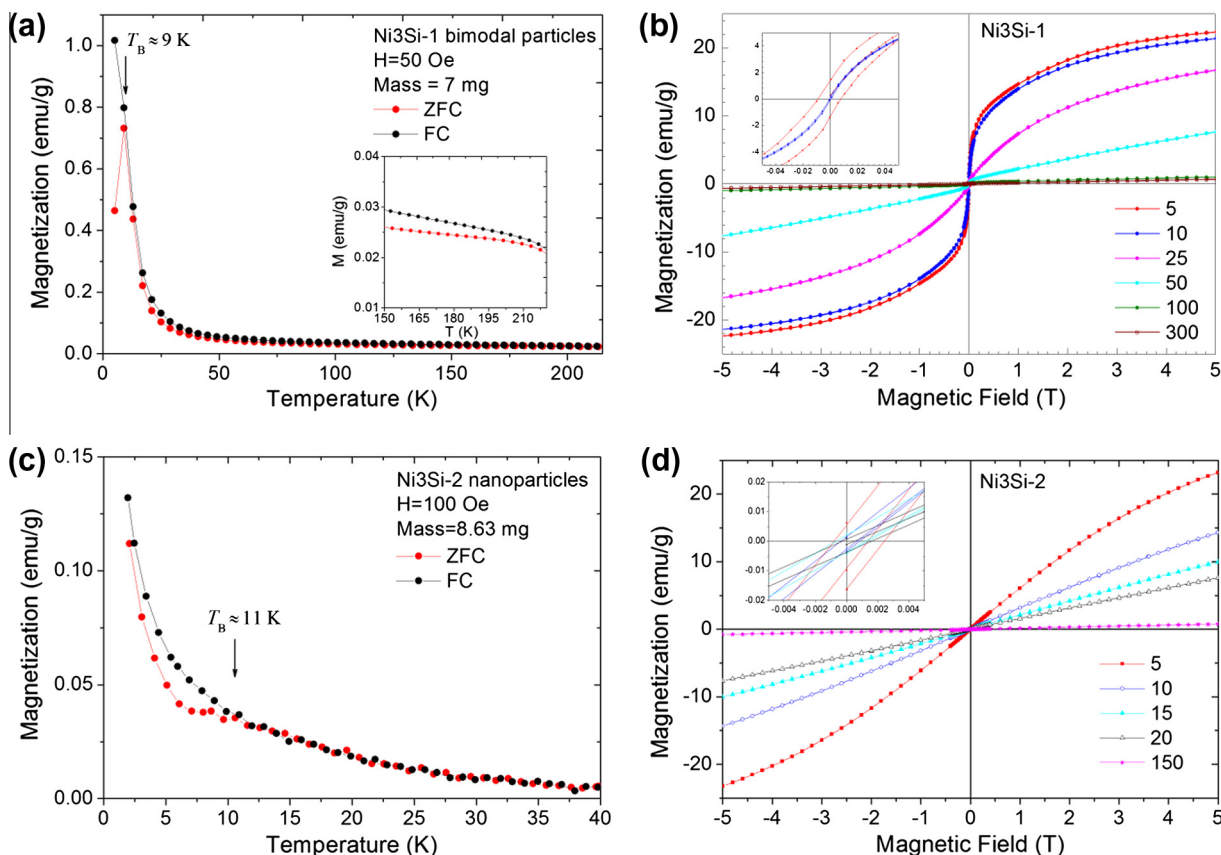


Fig. 6. Magnetization of nanoparticles. (a) ZFC and FC curves at 50 Oe and (b) $M(H)$ curves of the Ni₃Si(Al) bimodal particles (powder sample Ni₃Si-1). (c) ZFC and FC curves at 50 Oe and (d) $M(H)$ curves of the Ni₃Si nanoparticles (powder sample Ni₃Si-2).

determines the inter-particle distance and the magnetic dipole coupling between particles, which is responsible for the ferromagnetic hysteresis. Magnetic dipole coupling between neighboring nanoparticles is more effective below T_B when silica shell is thinner and can provide an additional demagnetization field, due to dipole coupling and formation of antiparallel alignment of neighboring particle moments which reduce the ferromagnetic hysteresis. The present results were inconclusive in determining the actual cause and more experiments are planned to resolve this in future.

4. Conclusions

In this article, an experimental investigation aiming at the understanding of the effect of size reduction on the structure and magnetic properties of different sizes of β_1 -Ni₃Si phase nanoparticles has been presented. It was demonstrated that by controlling the composition and heat treatment of the precursor alloy, the ESPD method is successful in downscaling nanoparticle size and in tuning their morphology without significantly modifying the nanoparticle lattice or the composition. The lattice misfit between precipitate and matrix in Ni–Si-based alloys can be influenced through ternary alloying additions (in this case Al) and thereby the size and shape of the precipitates can be controlled.

Nano-precipitates retain the L1₂ crystal structure, shape and size after extraction from the bulk alloy through electrochemical dissolution of the matrix. A small lattice contraction (<0.5%) is observed after removal of matrix's elastic constrain and it is due to the release of coherency strain with consequent crystal lattice relaxation. It may be pointed out that, as it was demonstrated in a previous publication [10], the lattice in the nanoparticles becomes strain-free after removal of the constraining matrix.

The magnetic properties of the precursor Ni–Si-based alloys from which the nanoparticles are extracted have been also characterized. Decreasing the nickel content in the Ni–Si-based alloys studied induces a decrease of saturation magnetization and an increase of Curie point, due to the increasing presence of β_1 -Ni₃Si phase. It demonstrates that in these alloys, the fcc nickel rich phase is responsible for the ferromagnetic character.

The extracted nanoparticles of β_1 -Ni₃Si phase exhibit a paramagnetic to ferromagnetic transition with low coercivity and saturation magnetization (>20 emu/g) at low temperatures (9–11 K) and this is interpreted as superparamagnetic behavior of single domain nanoparticles carrying a distribution of weak magnetic moments. A silica shell surrounding the nanoparticles can be an advantage for applications as it can protect from environmental degradation and also provide attachment sites for polymers, in case functionalization of particles surface is required for achieving stable colloidal suspensions. Additionally, the silica shell could offer thermal stability of nanoparticles assembled into thin films or composite materials with high-temperature processing. However, the oxidizing environment in which the silica shell grows can have an influence on the magnetic behavior of the nano-powders for the smaller particles, especially for weakly magnetic compounds like Ni₃Si with low anisotropy. The ESPD method is versatile and it can be used to produce intermetallic compounds with higher anisotropy in nano-size form which might be suitable for magnetic applications at room temperature.

Acknowledgments

Some of the core-shell nanoparticles were developed at the Institute of Applied Physics, ETH Zurich. Authors DM and GP are

grateful to Prof. em. Gernot Kosterz for his extensive support at the initial stage of this development. We gratefully acknowledge the collaboration of Aurélien Tournier-Fillon, Farzin Ziaiee Tabary, Jörg Patscheider, Erik Lewin, Daniel Schreier, Magdalena Parlinska and Rolf Erni at EMPA; Ilker Dincer and Eyup Duman at University of Ankara; Erwin Fischer and Fabio Krogh at ETH Zurich; Urs Gasser, Laszlo Almasy and Joachim Kohlbrecher at Paul Scherrer Institute. Financial support from the State Secretariat for Education and Research SER of Switzerland (Grant No. C11.0045) is gratefully acknowledged. Support is acknowledged from COST Action MP0903 “Nanoalloys as advanced materials: from structure to properties and applications”. The authors are indebted to SINQ (PSI Villigen, CH) and to MLZ (Garching, Germany) for providing beam time at the SANS-II and SPODI instruments, respectively.

References

- [1] H.-L. Zhang, F. Li, C. Liu, H.-M. Cheng, *Nanotechnology* 19 (2008) 165606.
- [2] A.T. Kuhn, H. Shalaby, D.W. Wakeman, *Corros. Sci.* 17 (1977) 833.
- [3] X. Chen, X. Liu, L. Wang, M. Li, C.T. Williams, C. Liang, *RSC Adv.* 3 (2013) 1728.
- [4] C.T. Liu, E.P. George, W.C. Oliver, *Intermetallics* 4 (1996) 77.
- [5] Y. Song, S. Jin, *Appl. Phys. Lett.* 90 (2007) 173122.
- [6] A.T. Dutra, P.L. Ferrandini, C.A.R. Costa, M.C. Gonçalves, R. Caram, *J. Alloys Comp.* 399 (2005) 202.
- [7] S. Van Dyck, L. Delaey, L. Froyen, L. Buekenhout, *Intermetallics* 5 (1997) 137.
- [8] J.S.C. Jang, C.H. Tsau, *J. Mater. Sci.* 28 (1993) 982.
- [9] G. Pigozzi, D. Mukherji, R. Gilles, B. Barbier, G. Kosterz, *Nanotechnology* 17 (2006) 4195.
- [10] G. Pigozzi, D. Mukherji, R. Gilles, P. Jencus, C. Siemers, *Nanotechnology* 20 (2009) 245704.
- [11] Y.P. Lee, Y.V. Kudryavtsev, Y.N. Makogon, E.P. Pavlova, J.Y. Rhee, *Eur. Phys. J. B – Condens. Matter Complex Syst.* 44 (2005) 431.
- [12] J.A. Kittl, A. Lauwers, C. Demeurisse, C. Vrancken, S. Kubicek, P. Absil, S. Biesemans, *Appl. Phys. Lett.* 90 (2007) 172107.
- [13] X. Chen, B. Zhang, C. Li, Z. Shao, D. Su, C.T. Williams, C. Liang, *Mater. Res. Bull.* (2011).
- [14] R.M. Bozorth, *Ferromagnetism*, Van Nostrand, 1951.
- [15] Y. Himuro, Y. Tanaka, N. Kamiya, I. Ohnuma, R. Kainuma, K. Ishida, *Intermetallics* 12 (2004) 635.
- [16] Q. Pankhurst, N. Thanh, S. Jones, J. Dobson, *J. Phys. Appl. Phys.* 42 (2009) 224001.
- [17] P. Strunz, D. Mukherji, G. Pigozzi, R. Gilles, T. Geue, K. Pranzas, *Appl. Phys.* 88 (2007) 277.
- [18] R. Gilles, D. Mukherji, M. Hoelzel, P. Strunz, D.M. Toebbens, B. Barbier, *Acta Mater.* 54 (2006) 1307.
- [19] R. Gilles, G. Artus, J. Saroun, H. Boysen, H. Fuess, *Phys. B Condens. Matter* 276–278 (2000) 87.
- [20] M. Hoelzel, A. Senyshyn, N. Juenke, H. Boysen, W. Schmahl, H. Fuess, *Nucl. Instrum. Methods Phys. Res. Sect. Accel. Spectrometers Detect. Assoc. Equip.* 667 (2012) 32.
- [21] P. Strunz, K. Mortensen, S. Janssen, *Phys. B Condens. Matter* 350 (2004) E783.
- [22] C.E. Williams, R.P. May, A. Guinier, in: E. Lifshin (Ed.), *Mater. Sci. Technol. Compr. Treat.*, 1994, pp. 611–656.
- [23] R.K. Heenan, J. Eastoe, *J. Appl. Crystallogr.* 33 (2000) 749.
- [24] K. Butter, A. Hoell, A. Wiedenmann, A.V. Petukhov, G.J. Vroege, *J. Appl. Crystallogr.* 37 (2004) 847.
- [25] Kohlbrecher J., Bressler I., SASFit, <<https://kur.web.psi.ch/sans1/SANSSoft/sasfit.html>>, n.d.
- [26] D. Mukherji, G. Pigozzi, F. Schmitz, O. Näth, J. Rösler, G. Kosterz, *Nanotechnology* 16 (2005) 2176.
- [27] M. Doi, *Prog. Mater. Sci.* 40 (1996) 79.
- [28] Y. Mishima, S. Ochiai, T. Suzuki, *Acta Met.* 33 (1985) 1161.
- [29] D. Mukherji, R. Müller, R. Gilles, P. Strunz, J. Rösler, G. Kosterz, *Nanotechnology* 15 (2004) 648.
- [30] T.I. Sigfusson, G.G. Lonzarich, *Phys. Scr.* 25 (1982) 720.
- [31] R.K. Rakshit, R.C. Budhani, *J. Phys. Appl. Phys.* 39 (2006) 1743.
- [32] D.C. Lee, F.V. Mikulec, J.M. Pelaez, B. Koo, B.A. Korgel, *J. Phys. Chem. B* 110 (2006) 11160.